


Art Checklist

Journal Code:		JCPH		
Article No:		6959		
	Disk Recd	Disk	Disk Usable	
Art #	Y/N	Format	Y/N	Remarks
Fig. 1	Y	PS	Y	
Fig. 2	Y	PS	Y	
Fig. 3	Y	PS	Y	
Fig. 4	Y	PS	Y	
Fig. 5	Y	PS	Y	
Fig. 6	Y	PS	Y	
Fig. 7	Y	PS	Y	
Fig. 8	Y	PS	Y	
Fig. 9	Y	PS	Y	
Fig. 10	Y	PS	Y	
Fig. 11	Y	PS	Y	
Fig. 12	Y	PS	Y	
Fig. 13	Y	PS	Y	
Fig. 14	Y	PS	Y	

Note:

1. .eps and .tif are preferred file formats.
2. Preferred resolution for line art is 600 dpi and that for Halftones is 300 dpi.
3. Art in the following formats is not supported: .jpeg, .gif, .ppt, .opj, .cdr, .bmp, .xls, .wmf and pdf.
4. Line weight should not be less than .27 pt.

Journal of Computational Physics **175**, 1–20 (2002)

doi:10.1006/jcph.2001.6959, available online at <http://www.idealibrary.com> on 

A Nonlinear Flux Split Method for Hyperbolic Conservation Laws

Youssef Stiriba

CERFACS/CFD Team, 42 Avenue Gaspard Coriolis, 31057 Toulouse Cedex 1, France

E-mail: Youssef.Stiriba@cerfacs.fr

Received January 19, 2001; revised September 14, 2001

We present and analyze the performance of a nonlinear, upwind flux split method for approximating solutions of hyperbolic conservation laws. The method is based on a new version of the single-state-approximate Riemann solver devised by Harten, Lax, and van Leer (HLL) and implemented by Einfeldt. It makes use of two-sided local characteristic variables to reduce the dissipation of HLL by introducing the flavor of HLL into the Steger–Warming flux vector splitting scheme. We use the characteristic decomposition and the method-of-lines approach to construct high-order versions of the first-order scheme and demonstrate their efficiency and robustness in several numerical tests. © 2002 Academic Press

Key Words: nonlinear systems of conservation laws; flux split schemes; high resolution.

1. INTRODUCTION

Recent years have known a great deal of progress in the development of numerical methods for solving hyperbolic systems of conservation laws that arise in compressible gas dynamic simulations, especially Euler equations. Most of the promising methods are the upwind numerical methods, which have proven to be robust and accurate for a wide range of problems of practical interest. A comprehensive review of such methods can be found elsewhere (e.g., in LeVeque [11], Toro [24], and references therein).

Basically, upwind methods can be divided into two main categories, namely flux-difference splitting (FDS) and flux-vector splitting (FVS) methods. FDS uses either exact or approximate Riemann solutions of the local Riemann problem between adjacent states to get a set of waves and speeds after field-by-field decomposition, and upwinding to distinguish between the influence of the left-going and right-going waves across the cell interfaces.

One of the most robust and popular FDS methods is the single-state-approximate Riemann solver attributed to Harten, Lax, and van Leer (HLL) [9]. It makes use of only

one intermediate wave state between two acoustic waves. With an appropriate choice of particle velocities, Einfeldt [4] has shown that this scheme (denoted HLL) satisfies all the important properties met by the Godunov method (e.g., positivity and entropy conditions). However it lacks information about isolated contact discontinuities [16].

The FVS methods ignore the interaction between the moving waves and split the physical flux into a right-going part and a left-going part. For instance, Steger and Warming [21] observed that the physical flux function of the inviscid Euler equations of gas dynamics is homogeneous of degree 1 and split the flux using the sign of the wave speeds. A drawback of such splitting is that it does not give good resolution near the sonic point, since the splitting does not behave continuously as the Mach number passes through 1. A differential FVS in subsonic regions has been constructed by van Leer [25], which gives noticeably better results.

Au: change okay?
(as meant?)

A different strategy [16] is to combine some desirable and complementary features of two or more solvers (e.g., a FDS and FVS). With this approach it is possible to construct a less-dissipative upwind scheme, and to control certain instabilities by changing the flavor of the dissipation mechanism rather than by using judiciously a small amount of artificial dissipation. However, such an approach has a user-problem: when and how to use one numerical flux function in preference to another.

In this paper we present a flux split algorithm in which the splitting between the left and right fluxes is done in a nonlinear, upwind way. The scheme can be interpreted as a hybridization between the Steger–Warming (SW) FVS scheme and the HLL solver, so that the two solvers are combined in a *nonlinear* way without using any adjustable parameters. Another interpretation of the scheme we propose is that it can be considered a new way of implementing the HLL scheme, using the transformation to characteristic fields. The method is combined with piecewise hyperbolic reconstruction (which uses hyperbola as reconstructing functions, see [14]) in space, and the total variation diminishing Runge–Kutta (RK) methods in time [20], to construct a high-order version of the first-order scheme. This new approach preserves positivity, provides accurate, oscillation-free, and well-behaved numerical approximation, and fixes a variety of numerical pathologies mentioned in [16].

The outline of the paper is as follows. In Section 2, we give a short overview of the HLL solver. In Section 3, we describe the nonlinear flux split algorithm and implementation details. In Section 4, we present numerical experiments in 1D and 2D to show the performance, efficiency, and robustness properties of our scheme.

2. THE HLL APPROXIMATE RIEMANN SOLVER—A SHORT OVERVIEW

We briefly overview the HLL schemes for the 1D hyperbolic system of conservation laws,

$$\mathbf{q}_t + \mathbf{f}(\mathbf{q})_x = 0, \quad (1)$$

subject to initial data

$$\mathbf{q}(x, 0) = \begin{cases} \mathbf{q}_L & \text{if } x < 0 \\ \mathbf{q}_R & \text{if } x > 0, \end{cases} \quad (2)$$

where

$$\mathbf{q} = \begin{pmatrix} \rho \\ m \\ E \end{pmatrix}, \quad \mathbf{f}(\mathbf{q}) = \begin{pmatrix} m \\ \rho u^2 + p \\ u(E + p) \end{pmatrix}, \quad (3)$$

and

$$E = \rho \left(e + \frac{1}{2} u^2 \right). \quad (4)$$

The variables t , x , ρ , u , e , E , and p denote time, space, density, velocity, internal energy, total energy, and pressure, respectively. Pressure is given by an equation of state, $p = p(\rho, e)$. We assume that the gas is a γ -law gas,

$$p = (\gamma - 1)\rho e, \quad (5)$$

where γ is the ratio of specific heats.

Consider a uniform grid in the $x - t$ plane, with mesh spacing Δx and a time-step Δt . The grid points are denoted by $x_i = i\Delta x$ and $t_n = n\Delta t$, and the computational cells are denoted by $C_i = (x_{i-1/2}, x_{i+1/2})$, with $x_{i\pm 1/2} = (i \pm 1/2)\Delta x$, $\forall i \in \mathcal{Z}$.

Harten *et al.* [9] approximate the Riemann problems (1) and (2) by assuming just two acoustic waves traveling with speeds λ_L and λ_R (see Fig. 1) and determine the averaged intermediate state q_M by integrating the conservation laws (1) over control volumes $C_i \times [t_n, t_{n+1}]$,

$$q_M = \frac{\lambda_R q_R - \lambda_L q_L - (f_R - f_L)}{\lambda_R - \lambda_L}. \quad (6)$$

The corresponding interface flux is given by integrating (1) over the control volume $[x_{i-1/2}, x_i] \times [t_n, t_{n+1}]$,

$$f_M = \frac{\lambda_L(-f_R + \lambda_R q_R)}{\lambda_R - \lambda_L} + \frac{\lambda_R(f_L - \lambda_L q_L)}{\lambda_R - \lambda_L}. \quad (7)$$

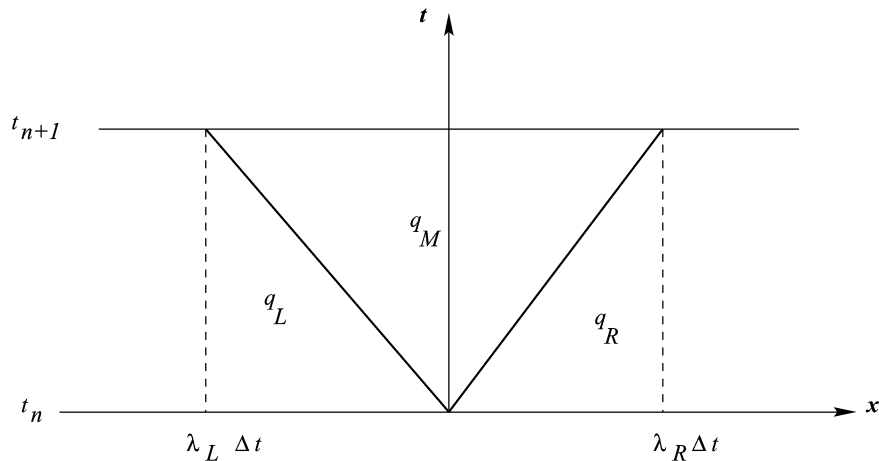


FIG. 1. Structure of the resulting Riemann solution in the $x - t$ plane.

Thus, the HLL numerical flux is

$$\mathbf{F}_{i+1/2}^{HLL} = \begin{cases} f_L & \text{if } \lambda_L > 0 \\ f_M & \text{if } \lambda_L < 0 < \lambda_R \\ f_R & \text{if } \lambda_R < 0. \end{cases} \quad (8)$$

The speeds λ_L and λ_R are approximations to the smallest and largest signal velocities of the exact Riemann solution. If there is only one wave traveling with one λ_L, λ_R , one obtains the exact solution. If we choose

Au: as meant? If not, pls. clarify sentence

$$\lambda_R = -\lambda_L = \frac{\Delta x}{\Delta t},$$

we recover the Lax–Friedrichs numerical flux function. However, the resulting scheme suffers from excessive numerical viscosity.

Einfeldt [4] suggested taking

$$\lambda_L = \min(\lambda_1(q_L), \lambda_1(q^{Roe})), \quad (9)$$

$$\lambda_R = \max(\lambda_3(q_R), \lambda_3(q^{Roe})), \quad (10)$$

where q^{Roe} is a mean state based on Roe linearization. This preserves positivity of density and internal energy, fixes entropy, and removes the carbuncle phenomena, but it lacks information about isolated contact discontinuities.

In the next section, we present a new way to implement the HLL Riemann solver, which leads to an upwind characteristic-based scheme that produces a well-behaved numerical approximation.

3. THE FLUX SPLIT ALGORITHM AND IMPLEMENTATION DETAILS

3.1. The First-Order Method

A fundamental tool in upwind FDS methods is the Riemann solver. In such an approach, the Riemann problem is solved exactly or approximately at each cell interface. This provides physical realism by correctly distinguishing between the influence of the moving information. The direction of information propagation is important for constructing stable and well-behaved upwind numerical schemes.

In our scheme, the local upwind directions are obtained by diagonalizing the flux Jacobian matrix rather than by solving directly a Riemann problem. This strategy has been used in flux-vector splitting and characteristic-based methods (see [3, 24, 11]). The flux Jacobian matrix is quite important to any characteristic-based method and in many real gas computations, since it determines the transformation to characteristic fields and thus the local propagation of independent waves, as well as what quantities are to be upwind differenced. Near an unresolved step gradient in the flow, in which the states \mathbf{Q}_L and \mathbf{Q}_R vary by a large amount from one node to the next, we use the two flux Jacobian matrices evaluated at these *physical* states in an upwind fashion rather than some artificial average, such as the Roe mean [18] or linear average, since the use of a single representative Jacobian seems to produce spurious oscillations in some circumstances (see [3]).

For a given interface cell, $x_{i+1/2}$, where we wish to compute the numerical flux, if there is no sonic point we use the upwind SW scheme. In the neighborhood of a sonic point, the

SW flux splitting gives poor resolution, since the splitting does not behave continuously as the Mach number passes through 1. In our flux, we add an intermediate state to produce a continuous transition in the characteristic fields corresponding to a characteristic velocity change (in sonic points that are included in the compression and the expansion waves). The method should be useful in some pathological cases, where the shock-capturing algorithms display continuously oscillations that project characteristics not belonging to the relevant characteristic family (shock or rarefaction family) (see, for example, [1, 22]). The care of this kind of problem, which in general will be generated, consists of adding a *judicious* (problem dependent) amount of numerical dissipation. But the question is when to add it. Our scheme switches the HLL flux dissipation *only* in the characteristic field corresponding to the characteristic wave sign change (see Section 4 for numerical results). The new flux is computed as follows: Let us denote by $\{\lambda_p(\mathbf{q})\}_{p=1}^3$, $\{L^p(\mathbf{q})\}_{p=1}^3$, and $\{R^p(\mathbf{q})\}_{p=1}^3$ the eigenvalues and the left and right eigenvectors of the Jacobian matrix $A(\mathbf{q}) \equiv \partial \mathbf{f} / \partial \mathbf{q}$, respectively. Consider a cell wall, $x_{i+1/2}$, where we have to evaluate the numerical flux function $\mathbf{F}_{i+1/2}^n$, at a given time-step n .

**Au: changes as meant?
If not, pls. clarify**

1. Decompose the left state, \mathbf{Q}_i , the right state, \mathbf{Q}_{i+1} , and the flux function evaluated at these states into characteristic variables,

$$\begin{aligned}\omega_i^p &= L^p(\mathbf{Q}_i) \cdot \mathbf{Q}_i, & \omega_{i+1}^p &= L^p(\mathbf{Q}_{i+1}) \cdot \mathbf{Q}_{i+1}, \\ \phi_i^p &= L^p(\mathbf{Q}_i) \cdot \mathbf{f}(\mathbf{Q}_i), & \phi_{i+1}^p &= L^p(\mathbf{Q}_{i+1}) \cdot \mathbf{f}(\mathbf{Q}_{i+1}),\end{aligned}$$

for $p = 1, 2, 3$. The characteristic velocities are denoted by $\lambda_L^p = \lambda^p(\mathbf{Q}_i)$, $\lambda_R^p = \lambda^p(\mathbf{Q}_{i+1})$, $p = 1, 2, 3$.

2. Find out if there is a compressible sonic point across the cell interface (i.e., if $\lambda_L^p \cdot \lambda_R^p \leq 0$).

3. If there is no sonic point, use upwinding to compute the numerical characteristic fluxes.

$$\begin{aligned}\text{If } \lambda_L^k > 0 \text{ and } \lambda_R^k > 0, & \text{ then } \phi_-^k = 0, \quad \phi_+^k = \phi_i^k. \\ \text{If } \lambda_L^k < 0 \text{ and } \lambda_R^k < 0, & \text{ then } \phi_-^k = \phi_{i+1}^k, \quad \phi_+^k = 0.\end{aligned}$$

Else consider an intermediate state and use (7) to compute the corresponding characteristic numerical fluxes.

$$\phi_-^k = \frac{\lambda_i^k (-\phi_{i+1}^k + \lambda_{i+1}^k \omega_{i+1}^k)}{\lambda_{i+1}^k - \lambda_i^k}, \quad (11)$$

$$\phi_+^k = \frac{\lambda_{i+1}^k (\phi_i^k - \lambda_i^k \omega_i^k)}{\lambda_{i+1}^k - \lambda_i^k}. \quad (12)$$

where

$$\lambda_i^k = \min(\lambda_L^1, \lambda_L^3, \lambda_R^1, \lambda_R^3) \quad (13)$$

and

$$\lambda_{i+1}^k = \max(\lambda_L^1, \lambda_L^3, \lambda_R^1, \lambda_R^3) \quad (14)$$

for $k = 1, 2, 3$.

The numerical flux function is obtained by multiplying by the right eigenvectors

$$\mathbf{F}_{j+1/2}^n := \mathbf{F}(\mathbf{Q}_i, \mathbf{Q}_{i+1}) = \mathbf{F}^+ + \mathbf{F}^-, \quad (15)$$

where

$$\mathbf{F}^+ = \sum_{p=1}^3 \phi_+^p R^p(\mathbf{Q}_i) \quad \text{and} \quad \mathbf{F}^- = \sum_{p=1}^3 \phi_-^p R^p(\mathbf{Q}_{i+1}). \quad (16)$$

The first-order accurate scheme has the conservative form

$$\mathbf{Q}_i^{n+1} = \mathbf{Q}_i^n - \frac{\Delta t}{\Delta x} (\mathbf{F}_{i+1/2}^n - \mathbf{F}_{i-1/2}^n)$$

to assure that discontinuities are captured by the scheme.

If the signal speeds $\lambda^p(\mathbf{Q}_i)$ and $\lambda^p(\mathbf{Q}_{i+1})$ are positive, then

$$\mathbf{F}(\mathbf{Q}_i, \mathbf{Q}_{i+1}) = \mathbf{f}(\mathbf{Q}_i), \quad (17)$$

and when the signal speeds are negative,

$$\mathbf{F}(\mathbf{Q}_i, \mathbf{Q}_{i+1}) = \mathbf{f}(\mathbf{Q}_{i+1}). \quad (18)$$

When an eigenvalue changes sign, the new flux function characteristic component is constructed from the HLL scalar numerical flux, which introduces additional dissipation to enforce an entropy condition in the case of a rarefaction wave (when $\lambda^p(\mathbf{Q}_i) < 0 < \lambda^p(\mathbf{Q}_{i+1})$), or in other circumstances, such as shock reflection (see Section 4). Thus, the present flux function corrects the lack of dissipation of SW-FVS by introducing the more-diffusive HLL constructed in [9] in characteristic fields determined by sonic points. This makes the resulting scheme less viscous than the HLL scheme.

We note that another treatment near sonic points was introduced by Roe [19], which breaks down expansion shocks, that appears in most upwind differencing schemes and eliminates the local pathology “glitches.” In our approach we treat sonic points that are included in the compression and the expansion waves.

3.2. High-Order Accuracy

Higher-order accuracy of the first-order scheme can be achieved by evaluating the right-flux Jacobian $A(\mathbf{q}_R)$ at the right-side-biased interpolation of the conserved variable \mathbf{q}_R , and the left-flux Jacobian $A(\mathbf{q}_L)$ at the left-side-biased interpolation of the conserved variable \mathbf{q}_L . Then we use the spectral information of the Jacobian matrices $A(\mathbf{q}_R)$ and $A(\mathbf{q}_L)$, separately, to reconstruct the characteristic fluxes ϕ_L^p and ϕ_R^p . We compute the flux vector in space, leaving the problem continuous in time. This gives an ordinary differential equation in time, namely

$$\frac{d\mathbf{q}}{dt} = -\frac{1}{\Delta x} (F_{i+1/2} - F_{i-1/2}), \quad (19)$$

where

$$F_{i+1/2} = F_{i+1/2}(\mathbf{q}_i(t), t) \quad (20)$$

is the numerical flux at the cell interface $x_{i+1/2}$ at time t , and we discretize in time using the total variation diminishing (TVD) Shu–Osher RK methods (TVD–RK) [20].

The states \mathbf{q}_L and \mathbf{q}_R are interpolated using the same type reconstruction procedure as is used for numerical characteristic fluxes. Our preferred approximation procedures are the third-order piecewise hyperbolic reconstruction (PHM) [14] and the WENO-5 [10, 12] methods, together with the third-order TVD–RK method.

3.3. Extension to Higher Dimension

We extend the present scheme to higher dimension using the standard dimension-by-dimension technique, so that the 1D algorithm applies in each spatial dimension.

Several remarks are in order.

1. We note that our scheme is a characteristic-based scheme that needs neither an exact **Au: change to 1 okay?** nor an approximate Riemann solution and avoids the use of artificial intermediate states.

2. There are other possible candidates for λ in (13) and (14)—one might use the wave-speed algorithm proposed by Davis [2] for estimating acoustic wave speeds in his HLL solver. For example,

$$\lambda_{i+1}^k = \max(|\lambda^1(\mathbf{Q}_i)|, |\lambda^1(\mathbf{Q}_{i+1})|, |\lambda^3(\mathbf{Q}_i)|, |\lambda^3(\mathbf{Q}_{i+1})|), \quad (21)$$

$$\lambda_i^k = -\lambda_{i+1}^k. \quad (22)$$

3. For a polytropic gas or a thermally (not necessarily perfect) gas, the physical flux is homogeneous of degree 1. For an arbitrary equilibrium real gas with EOS **Au: pls. clarify “thermally,” also, change in location of end parens as meant? If not, pls. clarify phrase**

$$p = p(\rho, e), \quad (23)$$

the physical flux no longer possesses the homogeneity property and we cannot find a natural real-gas extension of SW FVS and other FVS and FDS methods [13, 23]. This method extends easily to nonhomogeneous fluxes and especially to real gases without using additional assumptions or approximations. All we need is the flux matrix Jacobian and its eigensystem.

4. In our numerical experiments, we have observed that the PHM (which is formally third-order accurate) [14] performs better in many critical problems and is more local in the sense that the numerical flux uses only four points, in contrast to ENO-3 [20] or WENO-5 reconstructions, which depend on six-point values. Applying the present flux split algorithm in conjunction with the PHM approximation and third-order TVD–RK method gives a physically well-behaved, accurate, and robust numerical scheme, which is free of adjustable parameters and fixes a variety of numerical pathologies. **Au: changes as meant?**

4. NUMERICAL EXPERIMENTS

In this section, the proposed scheme for both one- and two-dimensional Euler equations is implemented. Several examples are chosen to show the performance of the first-order, ENO-2, ENO-4, PHM-3, and WENO-5 schemes.

4.1. One-Dimensional Tests

All of our one-dimensional problems are to be solved for $0 \leq x \leq 1$ and $t > 0$.

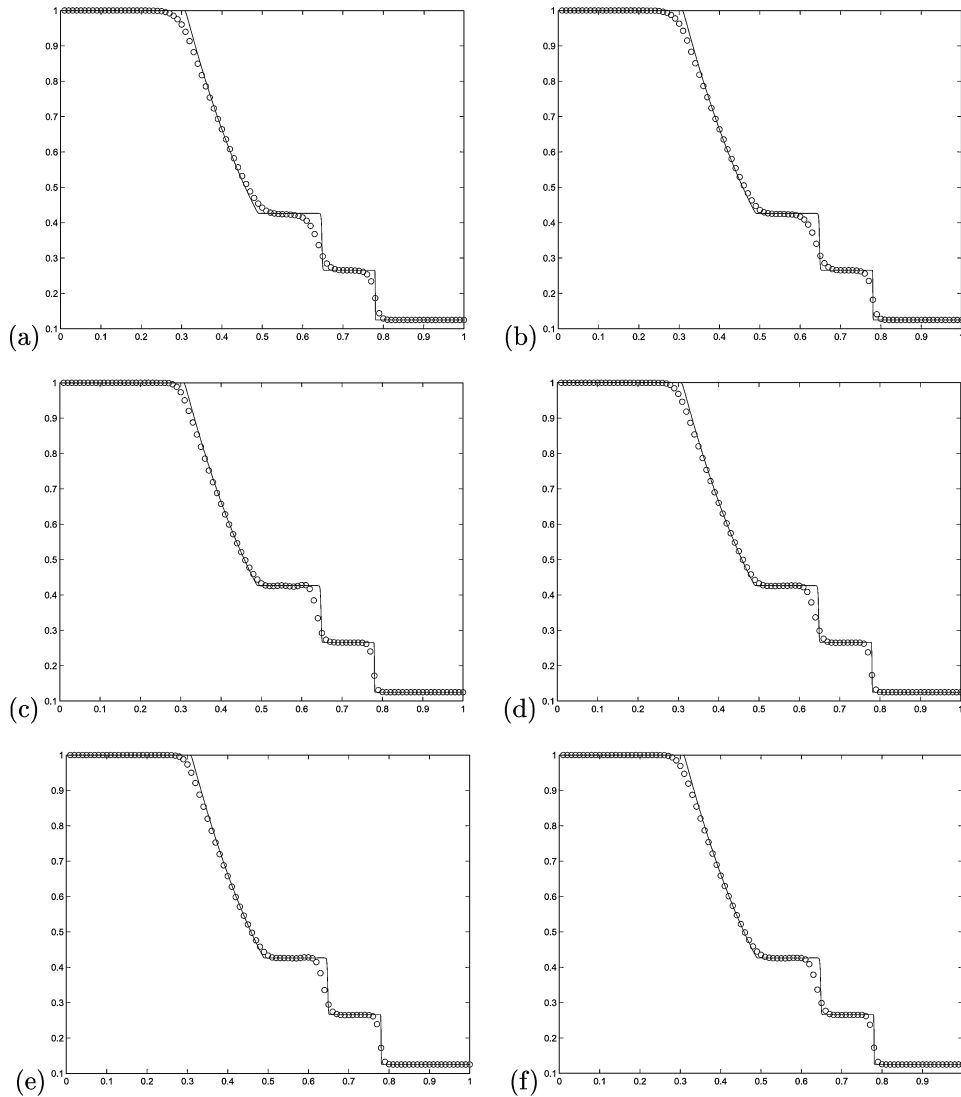


FIG. 2. Shock-tube problem. (a) ENO-2, (b) ENO-3, (c) ENO-4, (d) PHM-3, (e) WENO-5, and (f) PHM-Marquina.

EXAMPLE 1: Shock-tube problem. We begin with the Sod shock-tube problem. Initial data are

$$\begin{pmatrix} \rho \\ u \\ p \end{pmatrix} = \begin{cases} (1, 0, 1)^T, & x < 0.5 \\ (0.125, 0, 0.1)^T, & x > 0.5. \end{cases}$$

The solution contains four states separated by a shock, a contact surface, and a rarefaction wave. The numerical results, represented by circles, together with the exact solution, represented by solid lines, at time $t = 0.4$ on a 100-zone grid, are shown in Fig. 2. We can see that the three waves are well approximated, and the overall resolution improves as the order of the method increases. The present solver and Marquina's approach equipped with PHM or WENO reconstruction procedures perform well in this case.

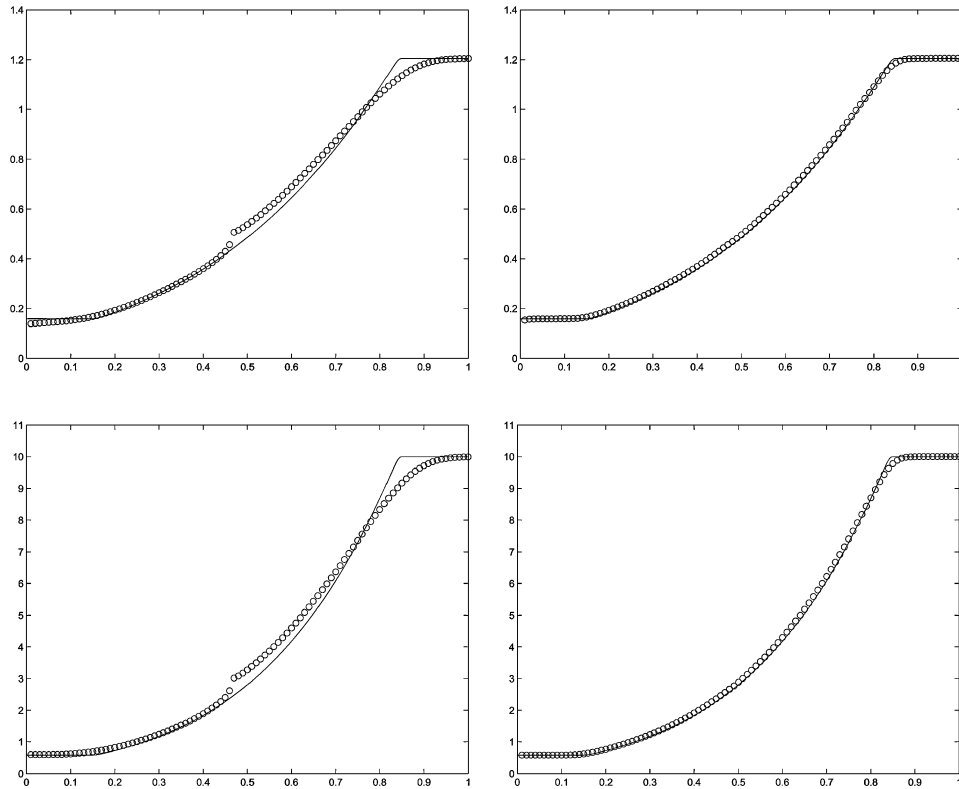


FIG. 3. Rarefaction wave with sonic point problem: first-order scheme (left), third-order scheme (right), density (top), and pressure (bottom).

EXAMPLE 2: Rarefaction wave with sonic point problem. In this example we reproduce the numerical test for the resolution of an entropy-violating stationary shock from [4] in Fig. 3. Initial data are

$$\begin{pmatrix} \rho \\ u \\ p \end{pmatrix} = \begin{cases} (1.205, 0, 10)^T, & x > 0.5 \\ (\rho_l, -(c_l + c_r), \rho_l c_l^2 / \gamma)^T, & x < 0.5, \end{cases}$$

where

$$\rho_l = 1.205 \cdot \left(\frac{c_l}{c_r} \right)^{\frac{2}{\gamma-1}},$$

$$c_l = \frac{3 - \gamma}{\gamma + 1} \cdot c_r.$$

Figure 3 shows the profiles of density and pressure with the first- and third-order schemes, at time $t = 1$ on a 100-zone grid. The numerical solution obtained with our first-order scheme shows a smaller $O(\Delta x)$ kink in the rarefaction wave identical to that of Godunov and HLLC methods in [4]. Such glitches, also called dogleg phenomena, are associated with many shock-capturing schemes [24]. We note that the sonic glitch disappears completely in the third-order PHM approximation.

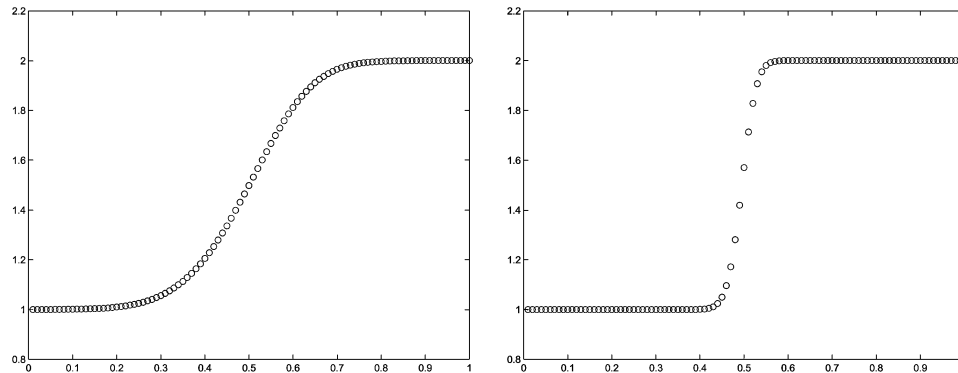


FIG. 4. Stationary-contact problem: first-order scheme (left) and third-order scheme (right).

EXAMPLE 3: Stationary contact discontinuity problem. Initial data are

$$\begin{pmatrix} \rho \\ u \\ P \end{pmatrix} = \begin{cases} (1, 0, 1)^T, & x < 0.5 \\ (2, 0, 1)^T, & x > 0.5. \end{cases}$$

The purpose of this example is to test the performance of the present flux for isolated stationary-contact discontinuity. This has important implications when solving Navier–Stokes equations in boundary layer, shear waves, and material interfaces. Figure 4 shows the results for the first- and third-order schemes. The present flux split Riemann solver diffuses the isolated stationary-contact wave, as do most flux-vector splitting schemes [24], and tends to smooth out the density with the number of time steps to similar levels, seen for example in Marquina’s scheme [3] or the HLL scheme [24]. This means that our scheme has built-in heat conduction (see [3]). The third-order scheme has less dissipation for stationary-contact discontinuity. A modification of our flux split algorithm to preserve the stationary-contact wave is under investigation.

Au: change as meant?
If not, pls. clarify

EXAMPLE 4: Shock-reflection problem. Initial data consist of a gas of constant density and pressure moving toward $x = 0$ in the computational domain,

$$(\rho, u, P) = (1, 1, 10^{-3}), \quad \text{and} \quad \gamma = \frac{5}{3}.$$

The boundary at $x = 0$ is a solid wall. The gas is thus compressed and heated, giving rise to a shock which propagates off the wall. The “overheating effects” occur in the first few zones near the wall [15, 3], when the shock reflects off the stationary solid wall. Following Noh [15], a numerical scheme with a built-in heat conduction mechanism will be able to dissipate the overheating.

Figure 5 shows numerical approximations obtained by the first- and third-order schemes. Although we observe a dip in the density (whose values are around 2% for the first-order scheme and 1.5% for the PHM scheme), this behavior is by no means as extreme as the one observed in other experiments (e.g., [8, 6]). We note that our scheme reduces the overheating and computes well the shock transition layer.

In Fig. 6, we compare the present solver and Marquina’s approach, combined with ENO-2, ENO-4, PHM, and WENO reconstruction procedures. We can observe that increasing the

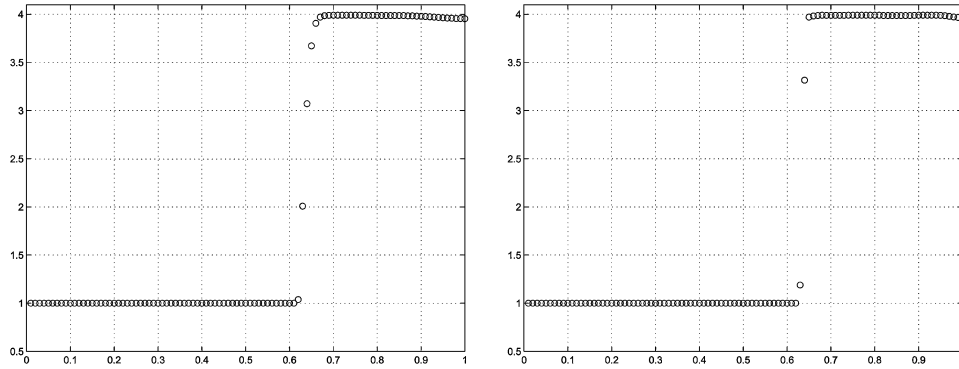


FIG. 5. Shock-reflection problem: first-order scheme (left) and third-order scheme (right).

order of the method reduces overheating with both solvers, and note that the use of WENO reconstruction leads to “underheating.” The third-order hyperbolic and ENO-2 extensions of the present scheme have better resolution at the solid wall and are able to reduce the “wall-heating error” in shock-reflection problems.

EXAMPLE 5: Slowly moving shock problem. The initial data we consider correspond to a Mach-3 shock moving to the right with a speed $s = 0.1096$ [16],

$$\mathbf{q} = \begin{cases} (3.86, -3.1266, 27.0913)^T, & x < 0.1 \\ (1, -3.44, 8.4168)^T, & x > 0.1. \end{cases}$$

In [1, 17, 16] and references therein, it has been observed that the numerical computation of slowly moving shock waves displays an anomalous behavior inherent to nonlinear systems: the numerical values in the postshock region display an oscillatory behavior which is completely nonphysical.

Numerical results computed by the present, Marquina, and HLLE schemes are displayed in Fig. 6. The solutions displayed correspond to 4000 time steps with $\Delta t/\Delta x = 0.1$. We clearly observe a long wavelength error in the postshock region in the HLLE scheme (see also Fig. 7). In our first-order scheme, the noise is undetectable, but the shock layer is less

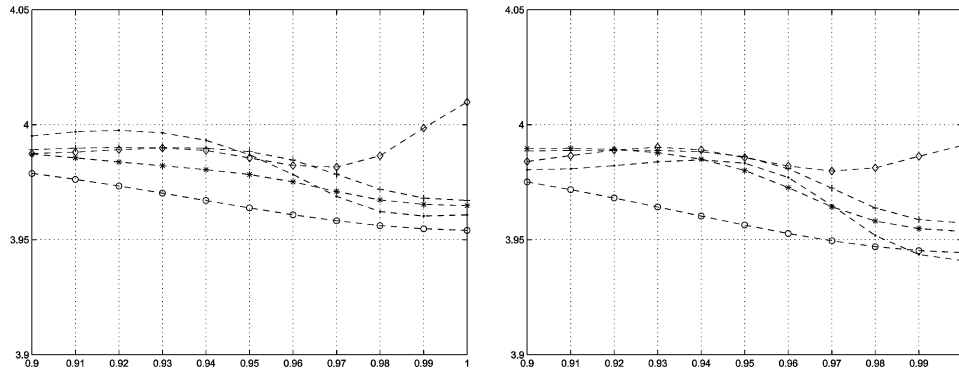
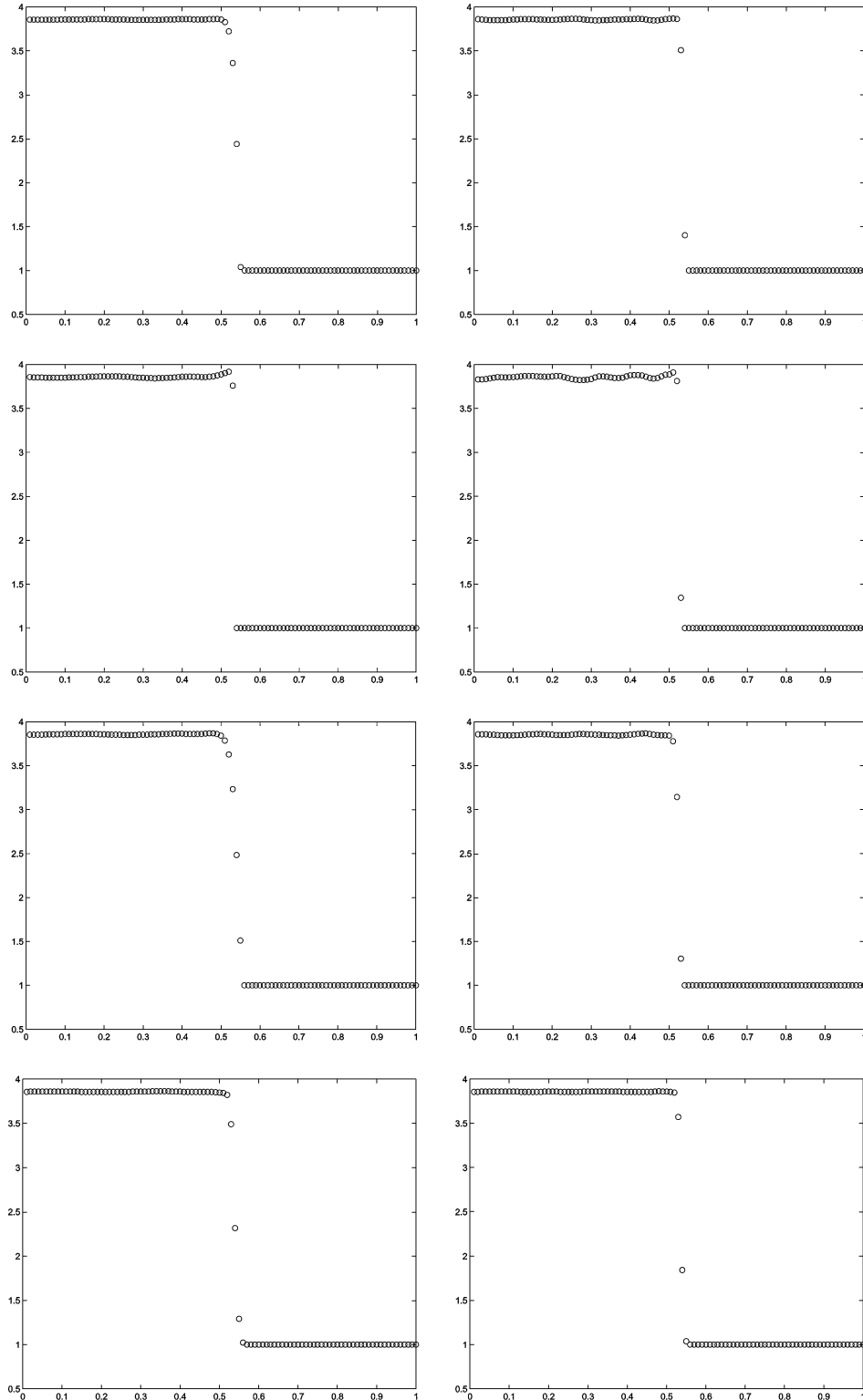


FIG. 6. Shock-reflection problem. Zoom at the rigid wall. (Left) Present scheme; (right) Marquina scheme. \circ , First-order; *, ENO-2; +, PHM; ---, ENO-4; \diamond , WENO.



Au:

changes as
meant? If
not, pls.
clarify

FIG. 7. Slowly moving shock problem: first-order scheme (left) and third-order scheme (right). The present method (top), the HLLC method (second from top), the Marquina scheme (second from bottom), and the modified scheme (bottom).

sharp than in the HLLE scheme. It was observed in [17] that this pathological behavior is worse when using high-order versions of numerical schemes. This is clearly appreciated in the PHM–HLLE scheme. Our third-order scheme as well as the PHM–Marquina scheme give results behind the shock that are as satisfactory as those obtained with many first-order schemes [22].

We modify our scheme by considering only the central part (i.e., (11) and (12)) with

$$\lambda_R^k = \min(|\lambda_L^p|, |\lambda_R^p|), \quad \lambda_L^p = -\lambda_R^p, \quad \text{for } p = 1, 2, 3. \quad (24)$$

We observe in Fig. 6 that the scheme works well and completely dissipates the oscillations in its first-order version as well as in its PHM-based third-order extension. More numerical experiments using this scheme are underway.

Au: changes okay?

EXAMPLE 6: Compression problem. Initial data are

$$\begin{pmatrix} \rho \\ u \\ p \end{pmatrix} = \begin{cases} (1, 4, 10^{-3})^T, & x < 0.5 \\ (1, -4, 10^{-3})^T, & x > 0.5. \end{cases}$$

where a highly compressed intermediate state is formed between two shock waves that propagate from the center in opposite directions. In the rigid-wall collision of the two slabs of the cold gas, the overheating effects appear. The results of our scheme and the Marquina and HLLE schemes are given in Figs. 8 and 9, indicating the good behavior and ability of our third-order scheme to dissipate the overheating. Similar results were obtained with ENO and WENO schemes (not presented here).

Au: as meant? If not, pls. cite figure 9 somewhere

EXAMPLE 7: Low-density and internal-energy Riemann problems. Initial data are [4]

$$\begin{pmatrix} \rho \\ u \\ p \end{pmatrix} = \begin{cases} (1, -2, 1)^T, & x < 0.5 \\ (1, 2, 1)^T, & x > 0.5. \end{cases}$$

The vacuum problem is a nonlinearizable Riemann problem where two rarefaction waves are formed and moving away from each other. These states are kinetic-energy rich, which causes instabilities for shock-capturing schemes [4]. Figure 10 displays the numerical results, where the first-order method gives results similar to those seen in [24] for the HLL scheme. It is worth mentioning that the ENO and WENO high reconstructions, as well as the third-order HLLE and Marquina schemes, blow up early in the first time steps, because density and internal energy become negative near the vacuum. However, our third-order scheme preserves positivity and gives good resolution.

Au: as meant? If not, pls. cite Fig. 10

4.2. Two-Dimensional Tests

We consider two-dimensional gamma law gas dynamics,

$$\mathbf{q}_t + \mathbf{f}(\mathbf{q})_x + \mathbf{g}(\mathbf{q})_y = 0, \quad (25)$$

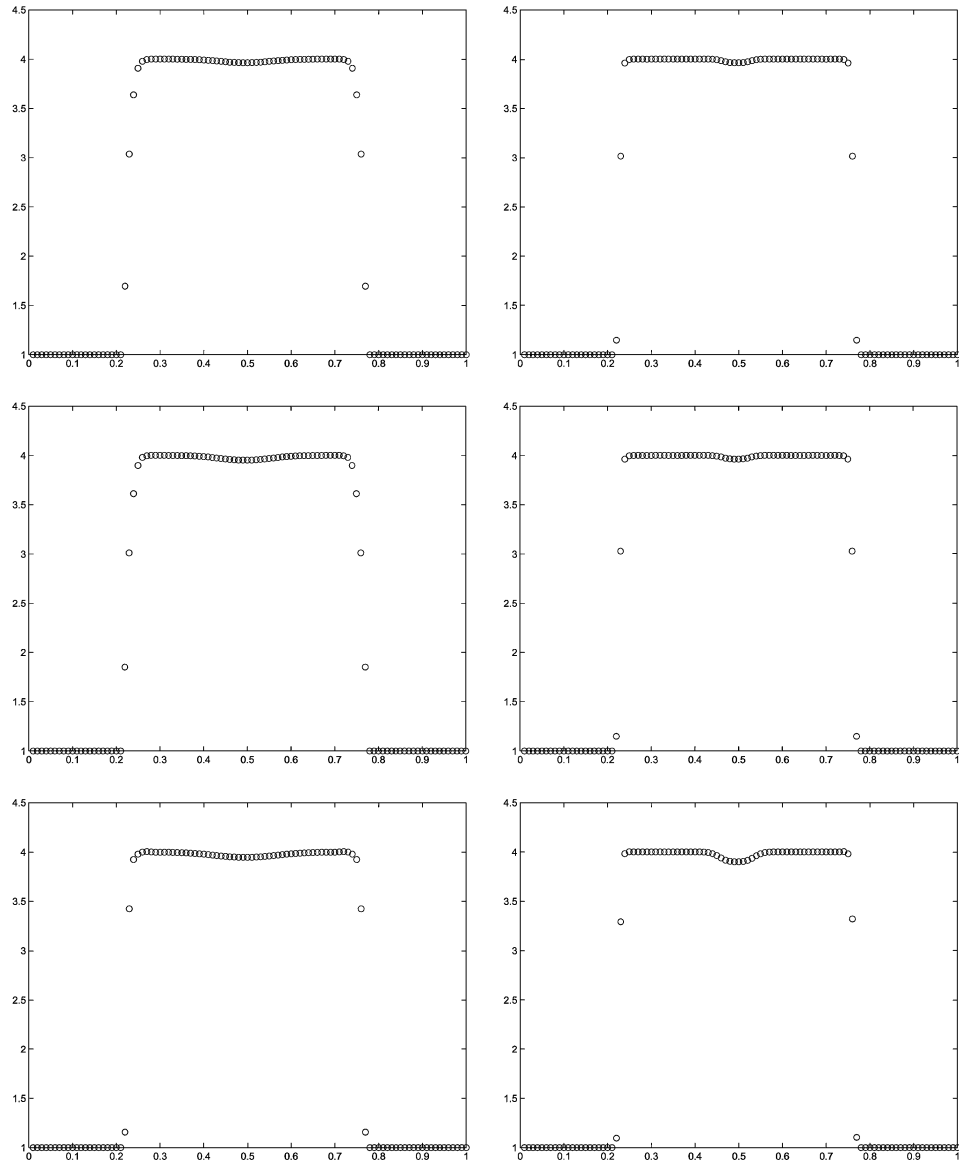


FIG. 8. Compression problem: first-order scheme (left) and third-order scheme (right). The present scheme (top), the Marquina scheme (middle), and the HLLE scheme (bottom).

$$\mathbf{q} = \begin{pmatrix} \rho \\ \rho u \\ \rho v \\ E \end{pmatrix}, \quad \mathbf{f}(\mathbf{q}) = \begin{pmatrix} \rho u \\ \rho u^2 + p \\ \rho uv \\ (E + p)u \end{pmatrix}, \quad \mathbf{g}(\mathbf{q}) = \begin{pmatrix} \rho v \\ \rho uv \\ \rho v^2 + p \\ (E + p)v \end{pmatrix}, \quad (26)$$

where

$$p = (\gamma - 1) \left(E - \frac{1}{2}(u^2 + v^2) \right). \quad (27)$$

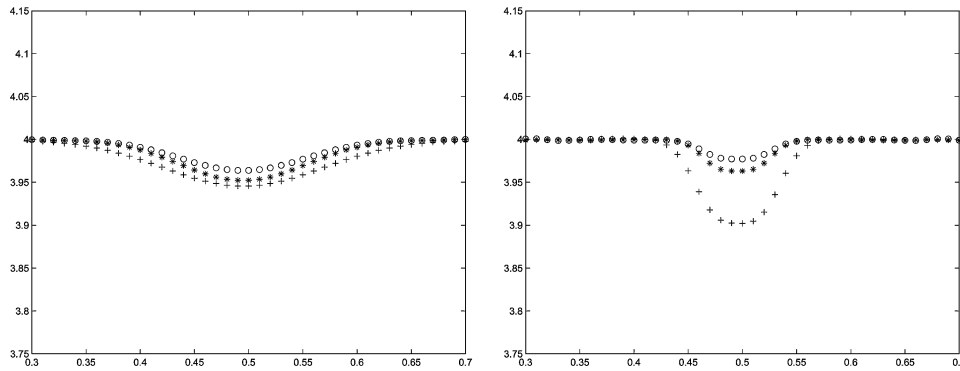


FIG. 9. Compression problem. Zoom at the rigid wall collision. (Right) First-order scheme; (left) third-order scheme. \circ , Present scheme; $*$, Marquina's scheme; $+$, HLLC scheme.

EXAMPLE 8: Flow past a forward-facing step. This test was used by Woodward and Colella [27] to compare and test the performance of numerical methods. The test problem involves a uniform Mach-3 flow in a wind tunnel containing a step. The tunnel is 3 units long and 1 unit wide. The step is 0.2 units high and is located 0.6 units from the left-hand side of the tunnel. An inflow boundary condition is applied at the left end of the computational domain, and outflow boundary conditions are applied at the right end. We apply reflecting

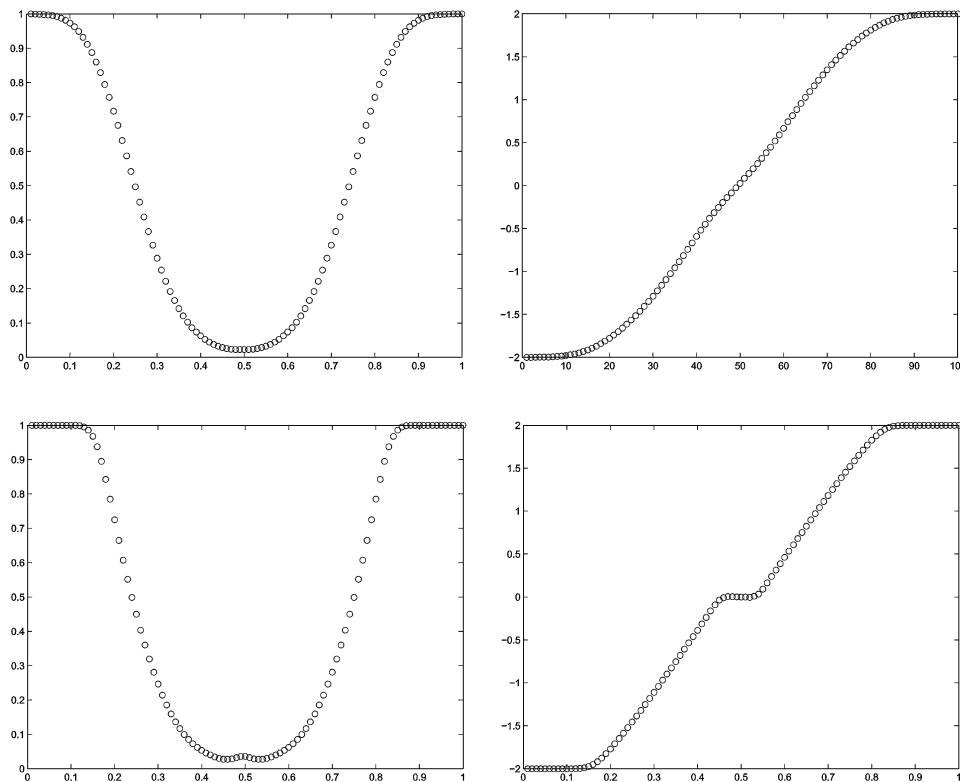


FIG. 10. Low-density and internal-energy Riemann problem: first-order scheme (top), third-order scheme (bottom), density (left), and pressure (right).

boundary conditions along the walls of the tunnel. The initial conditions for the gas in the tunnel are $\rho = 1.4$, $p = 1$, $u = 3$, and $v = 0$.

The density profile is the hardest to compute due to numerical errors generated at the corner of the step (which is a singular point of the flow), along the upper wall at the contact discontinuity, and at reflecting boundaries. We use the numerical treatment of [27, 3, 23] near the corner to fix the errors generated: a boundary layer in density of about one to two zones, the decrease of the two components of the velocity, as well as a spurious Mach stem at the bottom wall (see [23] for corner treatment using equilibrium equations of state).

We run the code, with an equally spaced grid $\Delta x = \Delta y = 1/80$, and display the numerical results when the unsteady flow has a rich and interesting structure. We display 30 equally spaced level curves between the minimum and maximum values of the computed density.

First-order, MUSCL [26], PHM, and WENO are used in our test, and the results are compared with those obtained with first-order- and WENO-Marquina's schemes. Figures 11

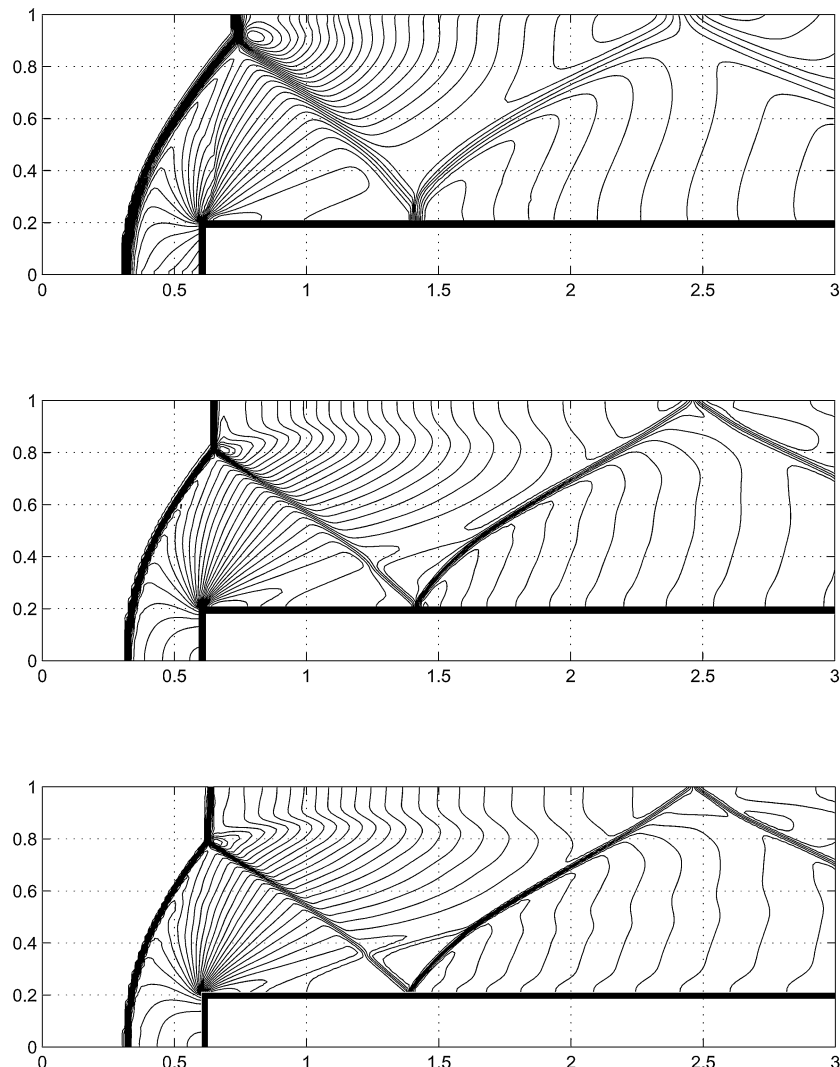


FIG. 11. Mach-3 step-flow problem. Contour plots of numerical approximations to the density by the first-order (top), the MUSCL (middle), and the PHM (bottom) schemes.

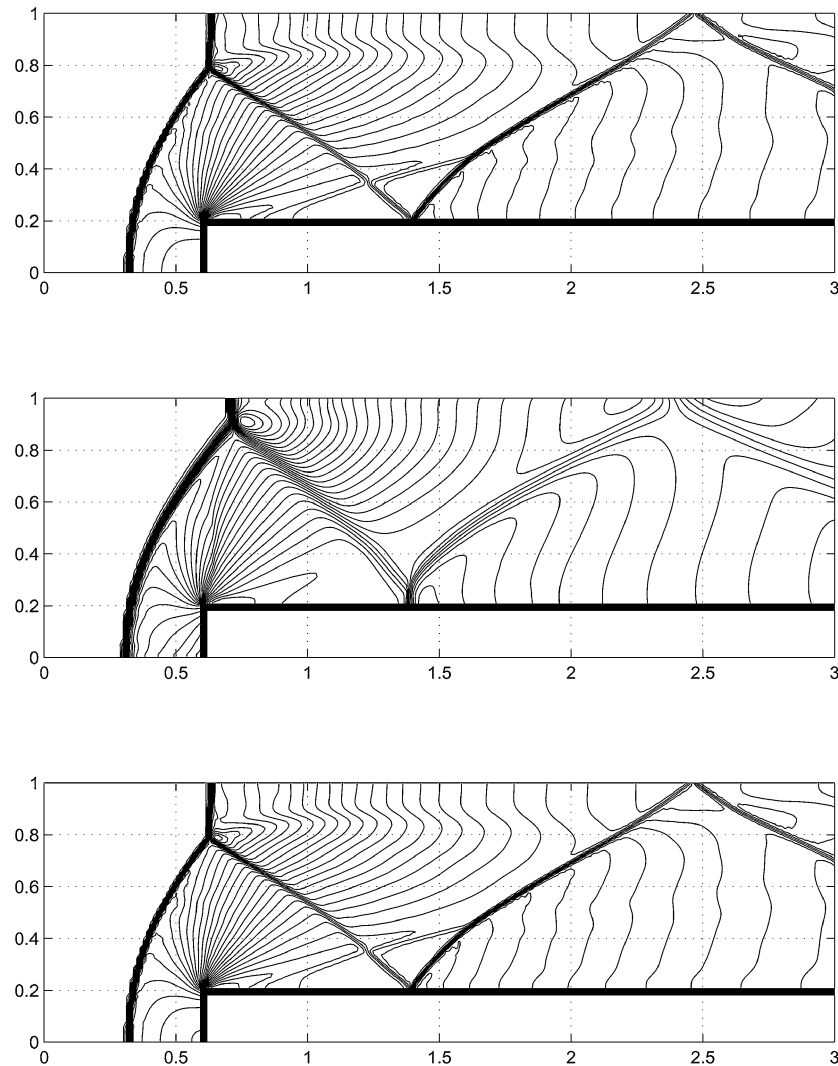


FIG. 12. Mach-3 step-flow problem. Contour plots of numerical approximations to the density by the WENO scheme (top), the first-order Marquina scheme (middle), and the WENO–Marquina scheme (bottom).

and 12 show the results. We can see that the shocks are well captured and accurate. The overheating errors are reduced (the level curves near the wall are more orthogonal). The entropy at the corner is preserved. The “kinked” Mach stem and the numerical noise related to the “carbuncle phenomena” (associated with nearly stationary shocks near the reflecting wall) are reduced. Also, we observe that the bow shock, the Mach stem, and the position of the reflected shock are consistent in all runs.

EXAMPLE 9: Double Mach reflection of a strong shock. The setup of problem [27] is as follows: a Mach-10 shock in air, $\gamma = 1.4$, initially makes a 60° angle a reflecting wall. The undisturbed air ahead of the shock has a density of 1.4 and a pressure of 1. We use the boundary condition described in [27]. The density is plotted in Figs. 13 and 14 with $\Delta x = \Delta y = 1/120$. We display 30 equally spaced level curves between the minimum and maximum values of the computed density, in $[0, 3] \times [0, 1]$.

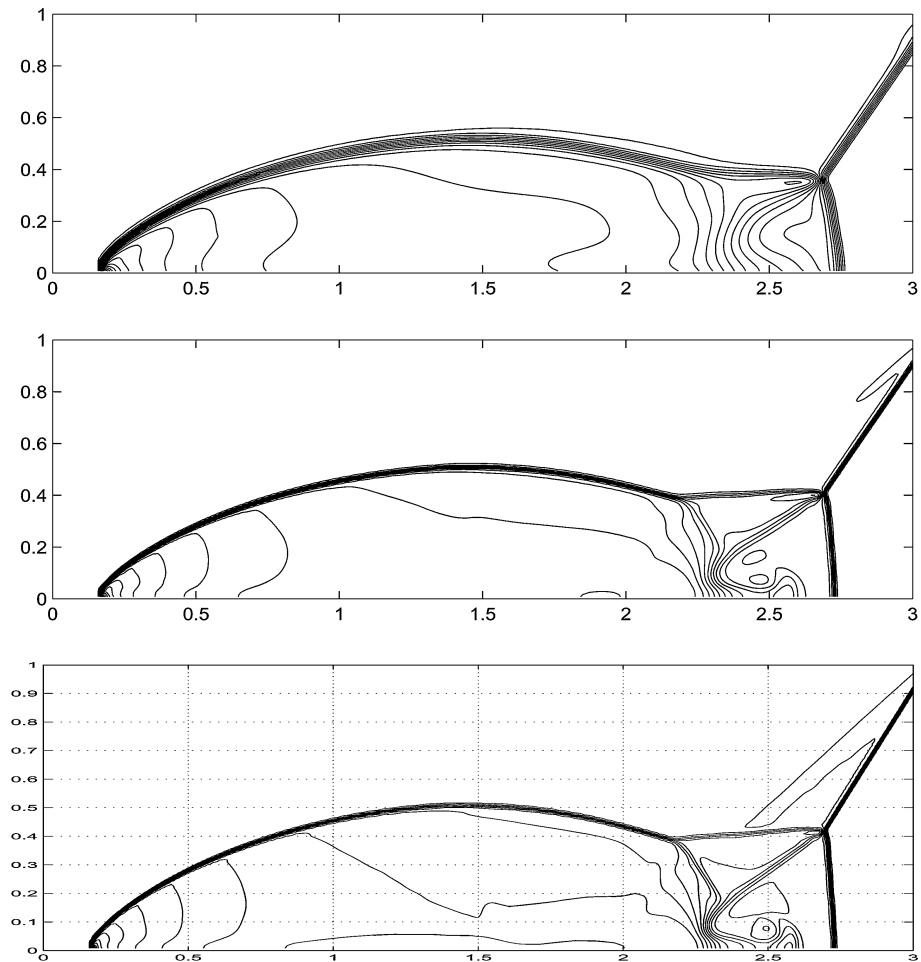


FIG. 13. Double-Mach reflection problem. Contour plots of numerical approximations to the density by the first-order (top), the MUSCL (middle), and the PHM (bottom) schemes.

We use first-order, MUSCL, PHM, and WENO in our test and compare the results with those obtained with first-order and WENO–Marquina schemes. We can see that the second Mach is well computed. The jet, formed when the flow of the denser fluid is deflected by a pressure gradient buildup in the region where the first contact discontinuity approaches the reflecting wall, is well captured. The curved reflected shock moves rapidly at its right end and does not move at all at its left end, which presents a computational difficulty for many finite-difference schemes. The PHM and WENO schemes combined with the present and Marquina solvers have good resolution without oscillations and resolve the two-Mach steam well.

5. CONCLUSION

This work presented a new third-order scheme based on a new flux split algorithm for compressible Euler equations of gas dynamics. The scheme is nonlinear, easy to implement, uses upwindness in local characteristic fields based on physical states, introduces the HLL

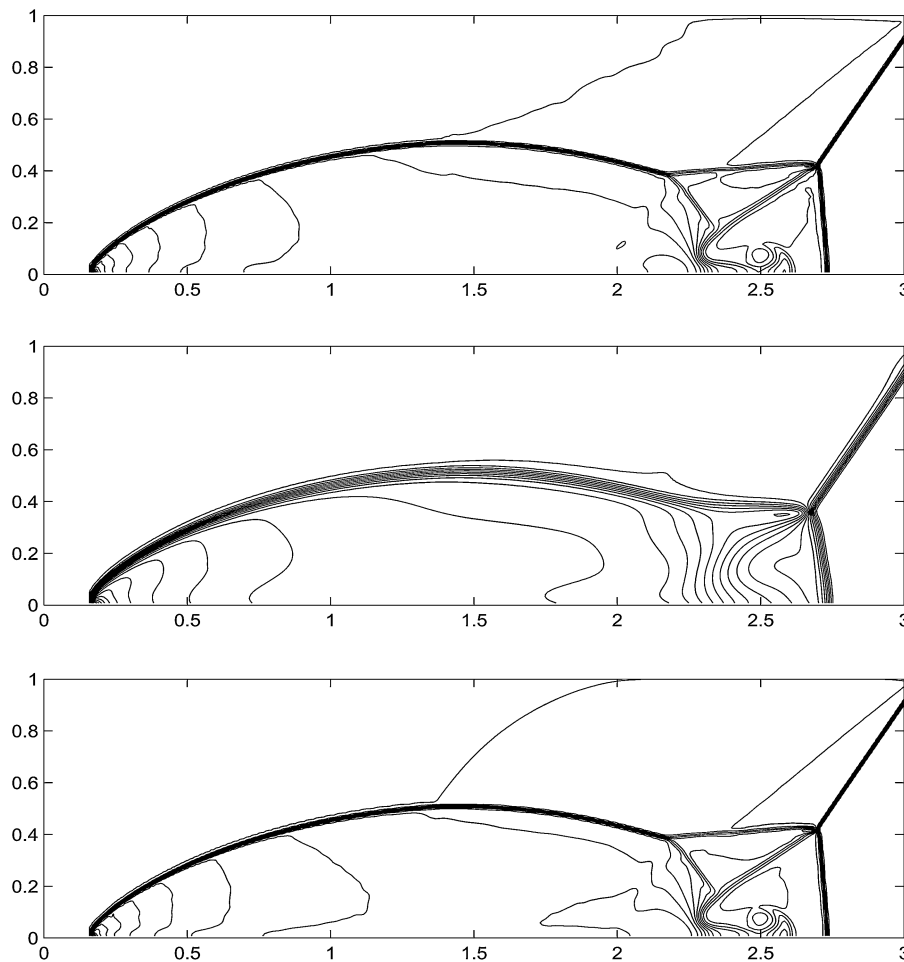


FIG. 14. Mach-3 step-flow problem. Contour plots of numerical approximations to the density by the WENO scheme (top), the first-order Marquina scheme (middle), and the WENO-Marquina scheme (bottom).

dissipation in a natural way, and extends easily to real-gas computations using directly the point values of thermodynamical derivatives without any assumptions or approximations. It can be considered another way to implement and switch the dissipation of the HLL approximate Riemann solver, using the sided characteristic fields.

Several numerical experiments, with other high-order reconstruction procedures and approximate Riemann solvers, were also presented. From the numerical results, it is clear that the third-order extension is a robust, efficient, and competitive numerical scheme.

ACKNOWLEDGMENT

Professor Antonio Marquina (Universidad de Valencia) is gratefully acknowledged for support and for stimulating discussions.

REFERENCES

1. M. Arora and P. Roe, On post-shock oscillations due to shock capturing schemes in unsteady flow, *J. Comput. Phys.* **130**, 1 (1997).

2. S. F. Davis, Simplified second-order Godunov-type methods, *SIAM J. Sci. Stat. Comput.* **9**, 445 (1988). **Au: Different journals as meant? (see also Refs. 14, 19)**
3. R. Donat and A. Marquina, Capturing shock reflections: An improved flux formula, *J. Comput. Phys.* **125**, 42 (1996).
4. B. Einfeldt, On Godunov-type methods for gas dynamics, *SIAM J. Sci. Comput.* **18**, 1553 (1997). **Au: Different journals as meant? (see also Refs. 14, 19)**
5. B. Einfeldt, C. D. Munz, P. L. Roe, and B. Sjogreen, On Godunov-type methods near low densities, *J. Comput. Phys.* **92**, 273 (1991).
6. R. Fedkiw, A. Marquina, and B. Merriman, An isobaric fix for the overheating problem in multimaterial compressible flows, *J. Comput. Phys.* **148**, 545 (1999).
7. R. Fedkiw, B. Merriman, R. Donat, and S. Osher, *The Penultimate Scheme for Systems of Conservation Laws: Finite Difference ENO with Marquina's Flux Splitting* (UCLA, 1996), CAM Report, pp. 96–18.
8. P. Glaister, An approximate linearized Riemann solver for the Euler equations for real gas, *J. Comput. Phys.* **74**, 382 (1988).
9. A. Harten, P. D. Lax, and B. van Leer, On upstream differencing and Godunov-type schemes for hyperbolic conservation laws, *SIAM Rev.* **23**, 35 (1983).
10. G. S. Jiang and C. W. Shu, Efficient implementation of weighted ENO schemes, *J. Comput. Phys.* **126**, 202 (1996).
11. R. J. LeVeque, *Numerical Methods for Conservation Laws* (Birkhäuser, Basel, 1990).
12. X. D. Liu, S. Osher, and T. Chan, Weighted essentially non-oscillatory schemes, *J. Comput. Phys.* **115**, 200 (1994).
13. M. S. Liu, B. van-Leer, and J. S. Shuen, Splitting of inviscid fluxes for real gases, *J. Comput. Phys.* **87**, 1 (1990).
14. A. Marquina, Local piecewise hyperbolic reconstruction of numerical fluxes for nonlinear scalar conservation laws, *SIAM J. Sci. Comput.* **15**, 892 (1994).
15. W. Noh, Errors for calculations of strong shocks using an artificial heat flux, *J. Comput. Phys.* **72**, 78 (1987).
16. J. J. Quirk, A contribution to the great Riemann debate, *Int. J. Numer. Methods Fluids* **18**, 555 (1994).
17. T. W. Roberts, The behavior of flux difference splitting schemes near slowly moving shock waves, *J. Comput. Phys.* **90**, 141 (1990).
18. P. L. Roe, Approximate Riemann solvers, parameter vectors, and difference schemes, *J. Comput. Phys.* **43**, 357 (1981).
19. P. L. Roe, Sonic flux formulae, *SIAM J. Sci. Comput.* **13**, 611 (1992).
20. C. W. Shu and S. Osher, Efficient implementation of essentially non-oscillatory shock capturing schemes, 2, *J. Comput. Phys.* **83**, 32 (1989).
21. J. L. Steger and R. F. Warming, Flux-vector splitting of the inviscid gas dynamic equations with applications to finite-difference methods, *J. Comput. Phys.* **40**, 489 (1981).
22. Y. Stiriba, *Study of Some Numerical Pathologies in Hyperbolic Systems of Conservation Laws*, Ph.D. thesis (Universidad de Valencia, 2000).
23. Y. Stiriba, A. Marquina, and R. Donat, *Equilibrium Real Gas Computations Using Marquina's Scheme*, GrAN Report, 00-01, available at <http://gata.uv.es/eng/reports.html>.
24. E. F. Toro, *Riemann Solvers and Numerical Methods for Fluid Dynamics* (Springer-Verlag, Berlin/New York, 1999), 2nd ed.
25. B. van Leer, *Flux-Vector Splitting for the Euler Equations*, Lecture Notes in Physics (Springer-Verlag, Berlin/New York, 1982), Vol. 170, p. 307. **Au: if article more than one page, pls. give inclusive pagination**
26. B. van Leer, Towards the ultimate difference scheme. V. A second order sequel to Godunov's method, *J. Comput. Phys.* **32**, 101 (1979).
27. P. Woodward and P. Colella, The numerical simulation of two-dimensional fluid flow with strong shock, *J. Comput. Phys.* **54**, 115 (1984).